NJC

PAPER

View Article Online
View Journal | View Issue

Cite this: *New J. Chem.*, 2024, **48**, 15428

Deep eutectic solvent assisted hydrothermal synthesis of photochromic and nontoxic tungsten oxide nanoparticles

Shephrah Olubusola Ogungbesan, *[a] Onome Ejeromedoghene, [b]
Yanina Moglie, [cde] Eduardo Buxaderas, [ce] Bingbing Cui,[a]
Rosemary Anwuli Adedokun,[f] Mulenga Kalulu,[a] Mopelola Abidemi Idowu,[g]
David Díaz Díaz *[cd] and Guodong Fu *[ab]

Received 2nd July 2024,
Accepted 12th August 2024

DOI: 10.1039/d4nj02995j

rsc.li/njc

In this work, hydrothermal methods and deep eutectic solvents were combined for the first time to prepare tungsten trioxide nanoparticles in an easy and green manner improving their optical and photochromic properties. Characterization of the synthesized nanoparticles was performed *via* Fourier transform infrared spectroscopy, X-ray diffraction, ultraviolet visible spectroscopy, scanning electron microscopy, energy dispersive X-ray, transform electron microscopy, dynamic light scattering, thermogravimetric analysis, and X-ray photoelectron spectroscopy. The average size of the spherical nanoparticles was *ca.* 1.83 nm as shown by TEM, and the nanoparticles exhibited high thermostability at least until 900 °C, and photostability and photosensitivity when they were exposed to UV light. Additionally, synthesized tungsten trioxide nanoparticles were found to be nontoxic with maximum cell viability observed even at 100 μg mL^{-1}, making them potential candidates for biomedical applications.

Open Access Article. Published on 13 August 2024. Downloaded on 2/17/2026 10:23:14 AM.
This article is licensed under a Creative Commons Attribution 3.0 Unported Licence.

Introduction

In recent years, the use and application of tungsten oxide nanoparticles have significantly increased.[1] This trend can be attributed to the unique properties and advantages of tungsten oxide nanoparticles compared with those of other metal oxide nanoparticles, which include exceptional electrochromic properties, excellent photocatalytic properties and gas sensing capabilities.[2] Tungsten oxide (WO_3) nanoparticles can undergo reversible color changes upon the application of an external stimulus.

The reversible color change of this material under light exposure is attributed to its particle size. Smaller nanoparticles offer more active sites for photoinduced reactions because of their higher surface area-to-volume ratio, enhancing light absorption and charge transfer processes. They also influence the electronic band structure and energy levels, resulting in an improved photochromic response compared with that of larger particles. Additionally, their shorter diffusion pathways accelerate charge separation and migration.[3] The significant color shift in tungsten oxide is pivotal for its biomedical applications, as it indicates alterations in the optical properties and electrical conductivities of the material.[4] This characteristic allows tungsten oxide to be utilized in targeted drug delivery systems. By integrating drugs into nanostructured tungsten oxide particles that respond to specific stimuli, such as light or pH changes, researchers can engineer smart drug carriers capable of releasing their payload only under desired conditions. This approach holds promise for minimizing side effects and improving therapeutic outcomes.[5]

Compared with other metal oxide nanoparticles, tungsten oxide nanoparticles exhibit faster response times, improved durability, and higher coloration efficiency, making them highly suitable for applications in smart windows, displays, and electrochromic devices.[6] Furthermore, the high photocatalytic activity of tungsten oxide nanoparticles can be attributed to their unique band structure and surface properties.[7] This

---

[a] *School of Chemistry and Chemical Engineering, Southeast University, 2 Southeast University Road, 211189 Nanjing, P. R. China. E-mail: 233189910@seu.edu.cn, fu7352@seu.edu.cn*
[b] *College of Chemistry, Chemical Engineering and Material Science Soochow University, 333 Ganjiang East Road, 215123 Suzhou, P. R. China*
[c] *Instituto Universitario de Bio-Orgánica Antonio González, Avda. Astrofísico Francisco Sánchez 2, La Laguna 38206, Tenerife, Spain. E-mail: dddiaz@ull.edu.es*
[d] *Departamento de Química Orgánica, Avda. Astrofísico Francisco Sánchez 3, La Laguna 38206, Tenerife, Spain*
[e] *Instituto de Química del Sur, INQUISUR (CONICET-UNS), Departamento de Química, Universidad Nacional del Sur, Avda. Alem 1253, 8000 Bahía Blanca, Argentina*
[f] *Department of Chemistry, Chrisland University Abeokuta, KM 3, Ajebo Road after FMC, 23409 Abeokuta, Nigeria*
[g] *Department of Chemistry, College of Physical Sciences, Federal University of Agriculture Abeokuta, Alabata Road, P.M. B 2240 Abeokuta, Nigeria*

This journal is © The Royal Society of Chemistry and the Centre National de la Recherche Scientifique 2024

Open Access Article. Published on 13 August 2024. Downloaded on 2/17/2026 10:23:14 AM.
This article is licensed under a Creative Commons Attribution 3.0 Unported Licence.

makes them promising materials for applications in solar energy (solar cells), water splitting (hydrogen production), and environmental remediation (photocatalytic degradation of organic dyes).[8] Tungsten oxide detects and distinguishes a wide range of gases, including nitrogen dioxide, hydrogen, and volatile organic compounds.[9] Moreover, the high sensitivity and selectivity of tungsten oxide nanoparticles for specific gases make them advantageous in gas sensing applications, such as air quality monitoring, industrial safety, and medical diagnostics.

Several methods, such as sol–gel, hydrothermal, chemical vapor deposition (CVD), deep eutectic solvent (DES), spray pyrolysis, solvothermal and pulsed laser ablation methods, have been explored for the synthesis of tungsten oxide nanoparticles.[10] Pulsed laser ablation in liquids was carried out by using a laser to ablate a tungsten target submerged in a liquid, resulting in the formation of WO_3 nanoparticles through rapid cooling and condensation.[11] The effects of the laser fluence and liquid environment are a concern in the use of this method. The difficulty of controlling the size distribution of nanoparticles is also a concern. The use of a solvent to dissolve precursor compounds under pressure at high temperature also results in the formation of tungsten oxide.[12] Padma and others reported the use of the spray pyrolysis method involving the atomization of precursor solutions into fine droplets, which are subsequently heated to form WO_3 nanoparticles.[13] In the CVD method, tungsten oxide nanoparticles are synthesized by the thermal decomposition of volatile precursor compounds in a controlled atmosphere, whereas in the hydrothermal method, the precursors react in an aqueous solution at high temperatures and pressures, leading to the formation of WO_3 nanoparticles.[14] On the other hand, the sol–gel method involves the hydrolysis and condensation of precursor compounds to form a gel, which is then thermally treated to obtain WO_3 nanoparticles.

The use of DESs is a relatively emerging area of research wherein these green solvents are used as templates or structure directing agents in the synthesis of tungsten oxide nanoparticles.[15] These subclasses of ionic liquids are formed by the combination of a hydrogen bond donor (HBD) and a hydrogen bond acceptor (HBA).[16] These solvents possess unique properties, such as low volatility, high thermal stability, and tunable properties, due to the use of HBD and HBA components. DES, which is used in the synthesis of tungsten oxide nanoparticles, acts as both the reaction medium and the precursor source. The HBD and HBA components of DESs can interact with tungsten-containing precursors, thereby facilitating the formation of tungsten oxide nanoparticles and modifying their surface properties.[17]

Despite the existing methods for synthesizing WO_3 nanoparticles, there is still a need to achieve a better control on critical properties such as particle size and photoresponsiveness, as well as to address sustainability concerns in terms of synthetic conditions. In order to fill this gap, we propose in this work the combination of hydrothermal method and DES for the synthesis of small and uniform WO_3 nanoparticles with enhanced photochromic properties. As far as we are aware, this is the first time that such combination is reported.

Experimental

Materials

All reagents were of analytical grade, supplied by Aladdin, Inc. (Shanghai, China), and were used as purchased without further purification. The salts included sodium tungstate dihydrate ($Na_2WO_4 \cdot 2H_2O$, $\geq$99.95%), sodium chloride (NaCl, $\geq$99.5%), glacial acetic acid 100%, ethylene glycol (EG, $\geq$99.8%) and choline chloride (ChCl, $>$98%).

Preparation of tungsten oxide nanoparticles

Tungsten oxide nanoparticles were prepared in a one-pot reaction. Prior to the preparation of WO_3, DES was prepared by dissolving 1.62 g (11.6 mmoles) of ChCl in 75 mL of 0.26 M NaCl and 5.40 mL of ethylene glycol (EG) and vigorously stirred for 5 min at 80 °C until all the particles were completely dissolved. After the formation of the clear DES, 1.70 g (5.2 mmoles) of $Na_2WO_4 \cdot 2H_2O$ were added while stirring continuously. The solution was maintained at pH 3.0 by adding glacial acetic acid to the drops, and the reaction flask was covered with foil to avoid interactions with light. The solution was then placed in an autoclave oven at 100 °C for 2 h for the hydrothermal reaction. The resulting whitish particles in the reaction flask were collected and washed with ethanol (3 × 10 mL) and water (3 × 10 mL), to remove DES. The resulting tungsten oxide nanoparticles were dried and stored for further characterization.[18,19]

Tests for photostability and photochromism

To evaluate the photostability of the synthesized WO_3 nanoparticles, photolysis was carried out. This procedure involved weighing 1.00 g of the synthesized WO_3 nanoparticles in a glass tube with a lid, and the tube was sealed with a well-padded box containing a Xe lamp at a fixed position. The lamp was switched on for 60 min, and the sample was exposed to radiation at irradiances of 0.052 W cm^{-2} and 0.039 W cm^{-2} *via* a xenon arc lamp.[20] A thermometer was attached to monitor the temperature at 5 min intervals, and after 20 min, the maximum temperature was 66.70 °C (see Fig. 7). At 10 min intervals from 0 min to 60 min, a portion of the sample was taken and subjected to UV-visible spectroscopic analysis.

Characterization of tungsten oxide nanoparticles

The pH meter used for pH monitoring was a Sartorius FE20-K plus. The films and other materials were dried in an electrothermal blast drying oven (PS-9040BS model). The morphology of the WO_3 nanoparticles was determined *via* field emission scanning electron microscopy (FE-SEM) (FE-Inspect F50). Fourier transform infrared (FTIR) spectra were collected on a Nicolet 8700 instrument by sensing the nanoparticle sample incorporated in the KBr pellet at a resolution of 4 cm^{-1} at wavenumbers ranging from 4000 cm^{-1} to 400 cm^{-1}, with an average of 32 scans. KBr pellets were prepared for FTIR analysis by oven drying the KBr salt, grinding to form powder, compressing the mixture, and placing the mixture under 10 tons to form the pellet, which was subsequently placed in the disc, after which the disc was inserted into the disc holder within the

Open Access Article. Published on 13 August 2024. Downloaded on 2/17/2026 10:23:14 AM.
This article is licensed under a Creative Commons Attribution 3.0 Unported Licence.

spectrophotometer for measurement. UV characterization was performed by dispersing the sample in ethanol to form a homogeneous whitish mixture typical of tungsten oxide nanoparticles, and the solution was analyzed *via* a UV 2600 spectrophotometer between 200 and 800 nm. Transmission electron microscopy (TEM) was performed on a Talos F200X, and the samples were dispersed in ethanol, ultrasonicated for 10 min, dotted on a transmission electron microscope (TEM) grid, left to dry for 5 min and placed in a sample holder, which was subsequently placed on the microscope. Elemental analysis was also carried out *via* energy dispersive X-ray (EDX) spectroscopy. Powder X-ray diffraction (PXRD) patterns of the samples were recorded with an Ultima IV (Kabuskiki Kaisha) instrument with a monochromatic Cu Kα radiation source (λ = 0.154056 nm), a tube voltage and an electric current of 40 kV and 40 mA, respectively; the scanning rate ranged from 5° to 60°; and the scan speed was 10° min^{-1}. A NETZSCH 209F3 instrument was used for thermogravimetric analysis (TGA) of the samples, which was performed under a nitrogen atmosphere at a heating rate of 10° min^{-1} and scanning from 30 °C to 800 °C. The materials were subjected to X-ray photoelectron spectroscopy (XPS) *via* a monochromatic Al Kα X-ray source (1486.71 eV photons) on an AXIS HIS 165 spectrophotometer (Kratos Analytical, Manchester, UK). A Shirley background was employed for the XPS fitting, and the carbon deposit peak at 284.7 eV served as the reference calibration standard. The XPS chamber vacuum was 10^{-9} mbar.

Cytotoxicity test

The sample solution was prepared to a final concentration of 500 μg mL^{-1} and sterilized by UV light. The prepared sample mixture (100 μL) was added to a 96-well plate, mixed with 100 μL of human skin fibroblast suspension (5 × 104 cells per mL), and incubated at 37 °C in a 5% CO_2 atmosphere for 24 h; 100 μL of 1× PBS was used as the blank control. Next, 10 μL of cell counting kit 8 (CCK-8) solution was added to the above mixture, which was subsequently incubated at 37 °C for 1 h. The optical density at 450 nm was subsequently measured *via* a microplate reader (Infinite F50, Tecan, Switzerland).[21] The cell viability formula is shown in eqn (1):

$$\text{Cell viability (\%)} = (d')/d_o \times 100\% \qquad (1)$$

where d_o is the optical density of the control sample and d' is the optical density of the different samples.

Results and discussion

Synthesis and characterization of the nanoparticles

The specific synthesis pathway and reaction mechanism for the preparation of WO_3 nanoparticles are dependent on the choice of DES precursor. The DES acts as a template or stabilizer, influencing the size, morphology, and crystalline structure of the resulting nanoparticles.

WO_3 nanoparticles were prepared *via* a simple one-pot synthesis comprising the hydrothermal reaction of $Na_2WO_4\cdot 2H_2O$ in a DES previously formed between choline chloride (ChCl), sodium chloride (NaCl) and ethylene glycol (EG). The mixture was subsequently placed in an autoclave oven at 100 °C for 2 h.[18,19]

The first step was the formation of the DES, which was achieved by heating a solution of ChCl, EG and NaCl. This resulted in the breaking down of the component's crystalline structure and the formation of a homogenous liquid. The addition of NaCl improved the conductivity and stability of the mixture. Upon addition of $Na_2WO_4\cdot 2H_2O$ to the prepared DES, it dissociated into $[WO_4]^{2-}$ ions under acidic conditions (pH = 3.0), and finally formed hydrated WO_3. The stabilizing and solvent properties of the DES aided the uniform dispersion of the ions. The hydrothermal reaction that occurs in the autoclave at 100 °C enables the formation of stable WO_3 nanoparticles. Moreover, the presence of the DES offers a special reaction medium that regulates the shape and size of the resultant nanoparticles, obtained as a white-off stable powder, through a consistent and controlled nucleation process.

The FTIR spectrum of the material revealed structural properties (Fig. 1), as indicated by the strong band at 3402 cm^{-1}. Water molecules intercalated with H_2O (W–OH) and symmetric stretching vibrations may be the cause of the absorption band in the 3404 cm^{-1} range. The two peaks at 1628 and 3404 cm^{-1} correspond to the intercalated water molecules (W–OH–H_2O) and symmetric stretching vibrations in the WO–OH and W–OH planes, respectively.[22] Additionally, the peaks at 1394 cm^{-1} and 1138 cm^{-1} are assigned to the W–OH stretching vibration. The peak at 962 cm^{-1} is ascribed to the W=O stretching vibration. The O–W–O stretching vibration is represented by broad transmittance peaks at 804 cm^{-1} and 750 cm^{-1}. In accordance with the W–O–W plane wagging mode, a peak at 573 cm^{-1} was found.[22] The absence of any different functional groups shows that the synthesized nanoparticles were free of contaminants.

Further structural characterization of the synthesized nanoparticles was carried out *via* X-ray photoelectron spectroscopy (XPS), as depicted in Fig. 2a. The full-scan high-resolution deconvolution of W(4f), O(1s), and C(1s) produced the XPS spectrum, which was used to assess the oxidation states. With a binding energy of 283.87 eV, the deconvolution peak at C(1s) in

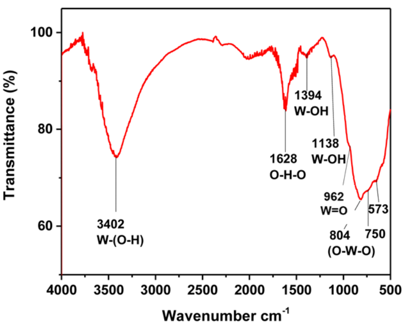

Fig. 1 FTIR spectrum of the WO_3 nanoparticles.

This journal is © The Royal Society of Chemistry and the Centre National de la Recherche Scientifique 2024

Open Access Article. Published on 13 August 2024. Downloaded on 2/17/2026 10:23:14 AM.
This article is licensed under a Creative Commons Attribution 3.0 Unported Licence.

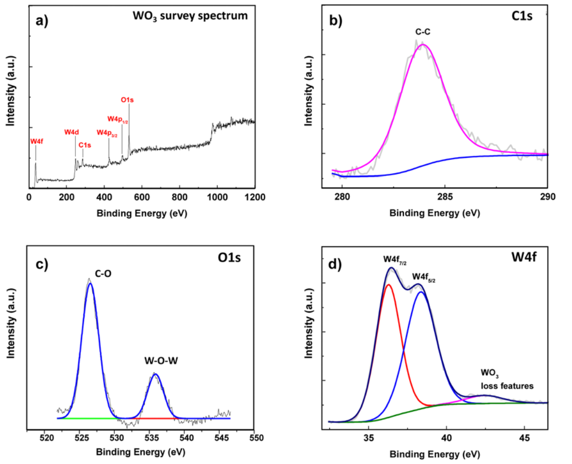

Fig. 2 (a) Low-resolution full XPS scan survey spectra. (b) High-resolution C(1s), (c) O(1s) and (d) W(4f) XPS spectrum of WO$_3$ nanoparticles.

Fig. 2b creates one peak that represents the C–C bond. The high-resolution spectrum of the O(1s) peak was divided into two peaks (Fig. 2c): the peak corresponding to adsorbed water (H_2O ads) or oxygen bound to carbon (C–O) and the W–O–W peak at 526.55 eV (with a low binding energy) and 535.88 eV were attributed to crystal lattice oxygen, with OH–W^{6+} bond states.[22] The calibration of all the adventitious carbon peaks from the XPS instrument is described in the reported literature and is supported by the energy difference of 2.16 eV between the W($4f_{7/2}$) and W($4f_{5/2}$) spin orbitals, which is in line with the theoretical value of WO$_3$ (Fig. 2d). W($4f_{7/2}$) exhibited a metallic state with oxygen adsorbed on the surface.[23] In summary, it is clear from the XPS data that W is present in the sample.

In Table 1, the surface atomic percentages of each component of the WO$_3$ nanoparticles are shown, as obtained *via* curve fitting of the XPS spectra.

Additionally, the elemental distribution determined *via* energy dispersive X-ray studies revealed that tungsten (W) made up 86.73% of the synthesized nanoparticles, oxygen 11.35%, and traces of sodium (1.82%) (Fig. 3a). W and O were present in significantly high amounts, and they made up the majority of the composition and were well distributed, as shown in the elemental mapping (Fig. 3b). The presence of these compounds in the materials could remarkably impact the light responsiveness as well as the compound's reduction–oxidation processes in photochromic reactions (Fig. 3c–e).[24]

Sample crystallinity and thermal stability studies

Table 1 Surface atomic percentages of the synthesized WO$_3$ nanoparticles

	Atomic%
C(1s)	15.08
O(1s)	60.39
W(4f)	24.52

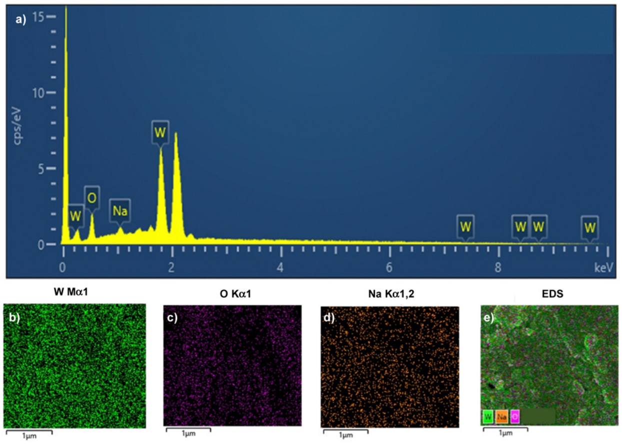

Fig. 3 (a) EDS elemental composition as a percentage of the mass distribution. Distribution of (b) W, (c) O, and (d) Na in WO$_3$ nanoparticles as depicted by elemental mapping. (e) Combined mapping of all the elements present in the synthesized nanoparticle X-ray photoelectron spectroscopy (XPS) spectra of the WO$_3$ nanoparticles.

The crystallinity of the as-prepared WO$_3$ nanoparticles was investigated *via* X-ray diffraction (XRD). The XRD pattern of the synthesized WO$_3$ nanoparticles in Fig. 4a shows that the phase has a monoclinic crystal structure, as the highest peak reflection was sharp and intense, indicating that no other phase transformations occurred. The observed crystal phases correspond to ICDD-PDF card no. 00-043-1035. The diffraction peaks with maximum relative intensities were observed at 23.12°, 28.62°, 33.26°, 40.84°, 49.94° and 54.16° and were attributed to the (002), (−112), (022), (311), (140) and (042) crystal planes, respectively. These peaks correspond to the crystallographic plane of tungsten trioxide and are commonly observed in its XRD pattern.[25] A crystal size of approximately 5 nm was calculated *via* Scherrer's formula, as shown in eqn (2):

$$D = 0.9\lambda/\beta\cos\theta \tag{2}$$

where D is the degree of crystallinity, λ is the machine wavelength (0.15418 nm), β is the full width at half maximum (FWHM, radius of 1.81009) and θ is the Bragg angle in degrees approximation (12°).

Moreover, the thermal stability of the synthesized WO$_3$ nanoparticles, as revealed by the TGA profile (Fig. 4b), reflects a high degree of thermal stability, with a total reduction in weight of less than 10% when exposed to high temperatures between 30 °C and 900 °C. Three notable phases of weight loss were observed in the TGA profile. The first weight loss (7%)

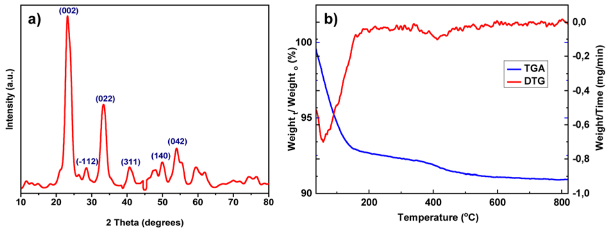

Fig. 4 (a) X-ray diffraction pattern of the WO$_3$ nanoparticles. (b) Thermogravimetric analysis (TG-DTA) curve of the synthesized nanoparticles.

Open Access Article. Published on 13 August 2024. Downloaded on 2/17/2026 10:23:14 AM.
This article is licensed under a Creative Commons Attribution 3.0 Unported Licence.

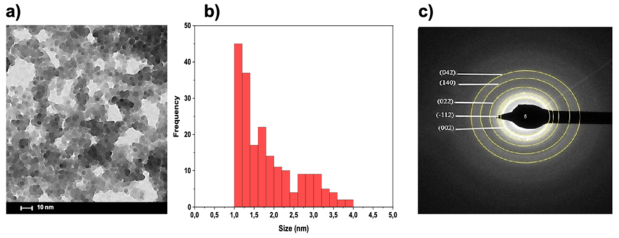

Fig. 5 (a) TEM micrograph of synthesized WO_3 nanoparticles and (b) size distribution of WO_3 nanoparticles. (c) SAED pattern of the synthesized WO_3.

occurred in the range of *ca.* 100–144 °C, which could be attributed to the loss of moisture physically absorbed on the surface of the WO_3 nanoparticles. The second stage of weight loss at 378 °C, with a 1% weight loss, could be associated with breakage of intermolecular bonds in the material or combustion of the organic residue in the material.[18]

Characterization and particle size distribution

The nanoparticle morphology and crystal structure were characterized *via* transmission electron microscopy (TEM). The TEM micrograph revealed the formation of well-distributed nanoparticles, as shown in Fig. 5a.† The image shows spherical particles that are 1.82 ± 0.7 nm in size.[22]

Reaffirming the presence of monoclinic WO_3 nanoparticles with crystal planes (002), (−112), (022), (140), and (042), as shown in the XRD pattern, the selected area electron diffraction (SAED) pattern (Fig. 5c) in accordance with ICDD-PDF card no. 00-043-1035 also showed a *d*-spacing value equivalent to these planes (Table 2).[26]

UV-visible (UV-vis) absorption studies and photochromic properties

UV absorption was observed in the UV spectrum during the nanoparticle investigation *via* a UV-Vis spectrophotometer. In Fig. 6a, the WO_3 nanoparticles exhibit an absorption edge at approximately 335 nm. After 60 min of monochromatic light exposure, the peak intensified. This shows that the sample had outstanding photostability. Electron excitation and delocalization between the atoms of the molecules may be the cause of the observed absorption of UV light. Fig. 6b illustrates the increase in the absorptive capacity of the synthesized material, which may be explained by the inherent motion of the photogenerated electrons and excitation from the lowest unoccupied W4d orbitals to the highest occupied molecular orbitals (HOMOs) in O 2p.[27]

Eqn (3) provides the absorption coefficient (α) for semiconducting materials such as WO_3, which is correlated with the optical bandgap energy.

$$(\alpha h\nu)^2 = A(h\nu - E_g) \tag{3}$$

Table 2 Interplanar spacing values of WO_3

$1/2r$ (nm^{-1})	1/2 (nm^{-1})	r (nm)	d-spacing (Å)	hkl
5.210	2.605	0.3839	3.839	002
6.435	3.218	0.3108	3.108	−112
7.431	3.716	0.2691	2.691	022
10.963	5.482	0.1824	1.824	140
2.890	1.445	0.1692	1.692	042

where h is Planck's constant; E_g is the optical bandgap; ν is the incident photon frequency; and A is a constant that is dependent on the electron and hole mobility of the material. Prior to being exposed to UV light, the material's obtained bandgap energy was 2.98 eV, and after exposure to UV light for the first 10 min, the bandgap energy reached 2.91 eV, as per the extrapolated Tauc plot (Fig. 6c) of the linear part of the $(\alpha h\nu)^2$ curve against the energy $h\nu$ axis. Subsequent curves for 20 min, 30 min, 40 min, 50 min and 60 min had band gaps of 2.89 eV, 2.85 eV, 2.89 eV, 2.77 eV, and 2.78 eV, respectively (Fig. 6d). The material's binding energy decreases in tandem with increasing UV light exposure time, which may be explained by the correlation between an increase in the number of oxygen vacancies, which produces more free electrons, and an increase in the material's optical and photochromic qualities.[28]

It should be emphasized that WO_3NP can absorb both UV and visible light. Using the equation for photon energy the wavelength corresponding to the energy band gap of 2.91 eV is 426.2 nm. This means that the nanoparticle can effectively absorb light, both at UV and Vis region, and has tendency to excite even to a longer wavelength as photocatalyst. When exposed to UV light over a period of time, WO_3 nanoparticles' bandgap decreases. This can be explained by a number of mechanisms, including surface defects, photoreduction, oxygen vacancy generation, and structural modifications. These procedures essentially lower the bandgap's energy by introducing new states within it.[18]

Photostability and photochromism

The photochromism of the synthesized WO_3 was confirmed when these nanoparticles were exposed to monochromatic light, and color changes and bleaching were observed. After five seconds of exposure, the light-absorbing nanoparticles turned from white to light blue (Fig. 6f). As time passed, the blue color became more intense. The synthesized nanoparticle samples that were dissolved (Fig. 6e) and dried (Fig. 6f) exhibited coloration and decolorization. After 15 s and 20 s, the color of the samples peaked. When the UV light was removed, the sample progressively returned to its original color after 42 and 35 s, respectively. These color changes and reversibility indicate redox reactions in photochromic materials, which is peculiar to the high percentage of tungsten and oxygen in the elemental distribution graph.

Colorimetric analysis

Colorimetry relies on human perception of color, which is influenced by the interaction of light with an object's surface.

---

† Less than 5% of the nanoparticles observed *via* TEM were found as aggregates of less than 70 nm.

This journal is © The Royal Society of Chemistry and the Centre National de la Recherche Scientifique 2024

Open Access Article. Published on 13 August 2024. Downloaded on 2/17/2026 10:23:14 AM.
This article is licensed under a Creative Commons Attribution 3.0 Unported Licence.

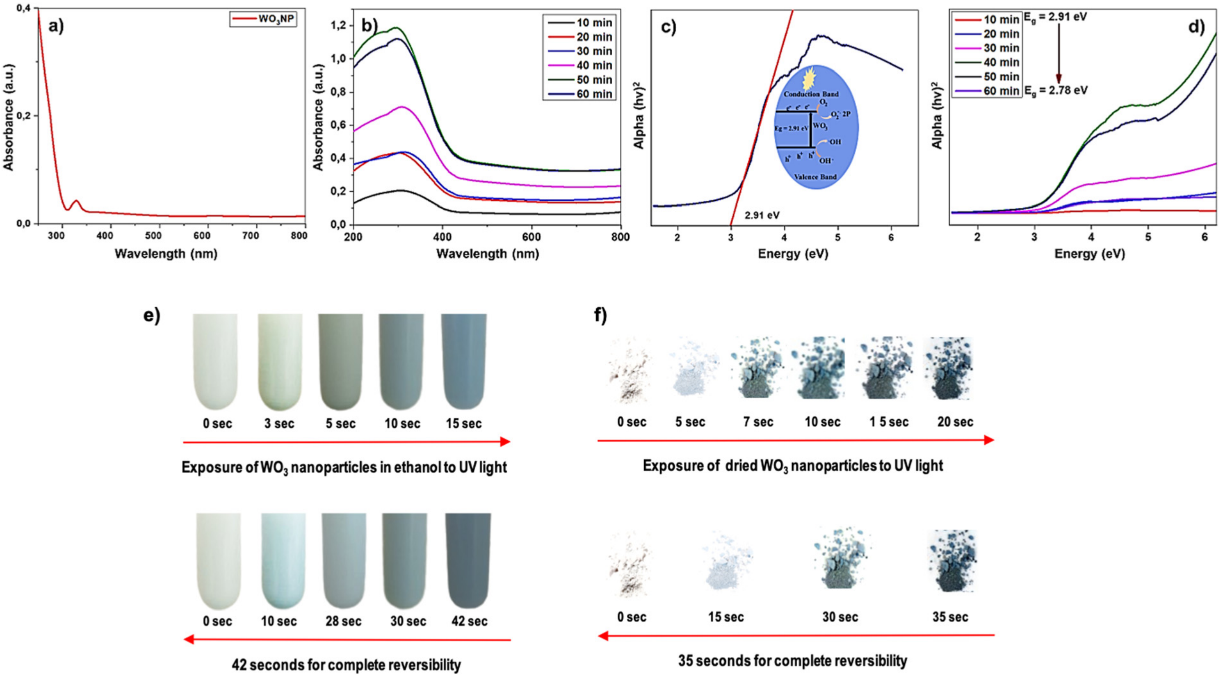

Fig. 6 (a) UV-Vis spectra of the nanoparticles before irradiation. (b) Absorption spectra after 0 min of irradiation for 60 min at 10 min intervals. (c) Tauc plot. (d) Spectrum of the band gap of the synthesized nanoparticles. (e) Response of the nanoparticles in ethanol to monochromatic light. (f) Response of the dried nanoparticles to monochromatic light.

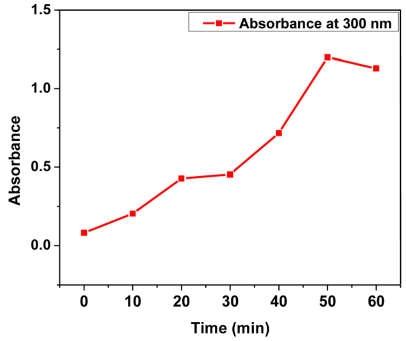

Fig. 7 Absorption of WO_3 nanoparticles at 300 nm over time.

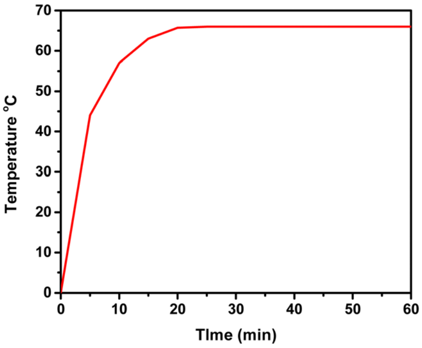

Fig. 8 Temperature over time during irradiation with a xenon arc lamp.

Different wavelengths of light are perceived as different colors, and colorimetry quantifies and standardizes these perceptions. The colorimetric analysis of this material is shown in Fig. 6e and f. Fig. 7 shows an increase in absorption at 300 nm over time, indicating the time-dependent behavior typical of photochromic materials. The photochromic mechanism of WO_3 nanoparticles involves the generation and trapping of charge carriers (electrons and holes) upon light absorption.[29] These trapped charges can modify the electronic structure of a material, leading to changes in its optical properties, such as the increased absorption shown in Fig. 7.

Fig. 8 shows the temperature distribution during the photoirradiation process at different times. After 5 min of irradiation, the temperature increases to 44 °C, and the temperature increase continues until after 20 min of irradiation, when the

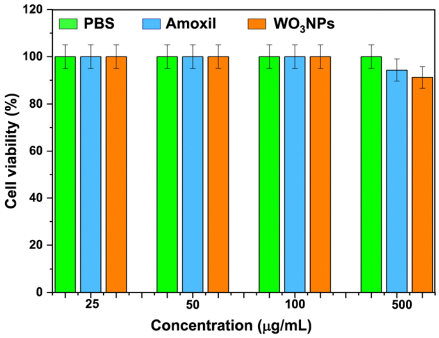

Fig. 9 Cell viability study of WO_3 NPs with corresponding control materials.

Table 3 Comparison of previous studies on the cytotoxicity of WO_3-based nanoparticles (NPs) with potential biomedical applications

NPs	Synthetic method	Cell line	Cell viability/concentration (μg mL^{-1})	Ref.
PVP-WO_3	Ion exchange	BJ fibroblasts	87.37%/400	31
WO_3H_2O	Pulse metal in liquid	Human alveolar basal epithelial A549	71.80%/400	32
Ct/Ag/WO_3	Sol–gel	B16F0	20%/500	33
$Ag_8W_4O_{16}$	Microwave irradiation	Human normal skin	100%/100	34
WO_3	DES-Hydrothermal	Human skin fibroblasts	91.9%/500	This work

Open Access Article. Published on 13 August 2024. Downloaded on 2/17/2026 10:23:14 AM. This article is licensed under a Creative Commons Attribution 3.0 Unported Licence.

temperature becomes constant at 66.7 °C. An increase in the exposure time to UV light led to an increase in the temperature and a decrease in the band gap. The photothermal stability of the synthesized WO_3 nanoparticles was confirmed.

Cytotoxicity

The results of the cell viability studies revealed that the maximum cell viability (100% cell survival) was reached at 25 μg mL^{-1}, 50 μg mL^{-1} and 100 μg mL^{-1} concentrations (Fig. 9). At 500 μg mL^{-1}, a toxicity value of *ca.* 8.80% was observed for the synthesized WO_3 nanoparticles, whereas a value of *ca.* 5.68% was measured when Amoxil was used as a control. Overall, the results revealed negligible toxicity with an average cell viability percentage of 91.2% over the whole range of concentrations.

Compared with other WO_3-based nanoparticles, our material showed significantly lower toxicity (Table 3). The low cytotoxicity that we observed even at a concentration of 500 μg mL^{-1} suggests that the synthesized WO_3 nanoparticles possess high biocompatibility and are not expected to cause any serious damage, significant immune response or rejection.[30]

Conclusions

The present study shows the successful synthesis of highly photoresponsive WO_3 nanoparticles *via* a combination of DES and a hydrothermal method. The hydrothermal process provides heat for nanoparticle crystallinity, while the presence of a deep eutectic solvent is crucial for regulating the segregation of particles. This simple and environmentally friendly methodology was found to be ideal for controlling the size of the nanoparticles, providing tiny and spherical nanoparticles with an average size of *ca.* 1.83 nm as shown by TEM. Moreover, these nanoparticles exhibited high thermostability between 30 and 900 °C. When the material was exposed to UV light, it demonstrated high photothermal stability, and photo reversibility of the dried and dissolved tungsten oxide. The study revealed that so-synthesized tungsten oxide nanoparticles showed no cytotoxicity at a concentration of 100 μg mL^{-1} and can thus potentially be used in biomedical applications.

Author contributions

Shephrah Olubusola Ogungbesan: conceptualization, research design, experimental, writing of original draft, reviewing data processing and analysis. Onome Ejeromedoghene: UV analysis, writing, reviewing and editing. Yanina Moglie and Eduardo Buxaderas: technical advice and results interpretation. Bingbing Cui: writing, reviewing and editing. Rosemary Anwuli Adedokun: experimental, analysis, writing, reviewing and editing. Mulenga Kalulu: writing, reviewing and editing. Mopelola Abidemi Idowu: writing, reviewing editing and supervision. David Díaz Díaz: conceptualization, funding acquisition, writing, reviewing and editing. Guodong Fu: conceptualization, funding acquisition, supervision.

Data availability

The datasets generated during and/or analysed during the current study are available from the authors on reasonable request.

Conflicts of interest

There are no conflicts to declare.

Acknowledgements

This work was supported by the National Natural Science Foundation of China under Grant 52073059. S.O.O. thanks Nanjing Municipal Government Scholarship, China. Y.M. thanks the Spanish Government for a María Zambrano postdoctoral grant. D.D.D. thanks the Spanish Government for the projects TED2021-132847BI00/AEI/10.13039/501100011033/Unión Europea NextGenerationEU/PRTR and PID2022-142118OB-I00/MCIN/AEI/10.13039/501100011033/UE. D.D.D. also thanks Nanotec, INTech, Cabildo de Tenerife and ULL for laboratory facilities. Authors also thank Prof. James N. O'Shea (University of Nottingham) for his feedback regarding XPS results.

Notes and references

1 P. A. Shinde and S. C. Jun, *ChemSusChem*, 2020, **13**, 11.

2 (*a*) S. Cong, F. Geng and Z. Zhao, *Adv. Mater.*, 2016, **28**, 10518; (*b*) A. Sharma, A. K. Saini, N. Kumar, N. Tejwan, T. A. Singh, V. K. Thakur and J. Das, *Surf. Interfaces*, 2022, **28**, 101641.

3 S. Wang, W. Fan, Z. Liu, A. Yu and X. Jiang, *J. Mater. Chem. C*, 2018, **6**, 191.

4 J. Bentley, S. Desai and B. P. Bastakoti, *Chem. – Eur. J.*, 2021, **27**, 9241.

5 F. O. Osazee, K. E. Mokobia and I. H. Ifijen, *Biomed. Mater. Dev.*, 2023, **2**, 614.

This journal is © The Royal Society of Chemistry and the Centre National de la Recherche Scientifique 2024

Open Access Article. Published on 13 August 2024. Downloaded on 2/17/2026 10:23:14 AM.
This article is licensed under a Creative Commons Attribution 3.0 Unported Licence.

6 (*a*) M. Arslan, Y. E. Firat, S. R. Tokgöz and A. Peksoz, *Ceram. Int.*, 2021, **47**, 32570; (*b*) S. J. Lee, D. S. Choi, S. H. Kang, W. S. Yang, S. Nahm, S. H. Han and T. Kim, *ACS Sustainable Chem. Eng.*, 2019, **7**, 7111.

7 (*a*) P. Shandilya, S. Sambyal, R. Sharma, P. Mandyal and B. Fang, *J. Hazard. Mater.*, 2022, **428**, 128218; (*b*) R. Rong and L. Wang, *J. Alloys Compd.*, 2021, **850**, 156742; (*c*) T. Subramani, G. Thimmarayan, B. Balraj, N. Chandrasekar, M. Palanisamy, S. K. Nagarajan, S. Amirtharajan, M. Kumar and C. Sivakumar, *Inorg. Chem. Commun.*, 2022, **142**, 109709.

8 J. C. Murillo-Sierra, A. Hernández-Ramírez, L. Hinojosa-Reyes and J. L. Guzmán-Mar, *Chem. Eng. J. Adv.*, 2021, **5**, 100070.

9 (*a*) X. An, Z. Shang, Y. Bai, H. Liu and J. Qu, *ACS Sustainable Chem. Eng.*, 2019, **7**, 19902; (*b*) K. R. Reyes-Gil and D. B. Robinson, *ACS App. Mater. Interfaces*, 2013, **5**, 12400.

10 (*a*) V. Galstyan, A. D'Arco, M. Di Fabrizio, N. Poli, S. Lupi and E. Comini, *Rev. Anal. Chem.*, 2021, **40**, 33; (*b*) A. Yadav, P. Singh and G. Gupta, *Environ. Sci.: Nano*, 2022, **9**, 40.

11 U. Onwukwe, L. Anguilano and P. Sermon, *Oxide Electronics*, VCH, Weinheim, 2021, p. 453.

12 (*a*) X. Fuku, K. Kaviyarasu, N. Matinise and M. Maaza, *Nanoscale Res. Lett.*, 2016, **11**, 386; (*b*) P. Gutpa, H. Shaik, K. Naveen Kumar and S. A. Sattar, *Mater. Sci. Semicond. Process.*, 2022, **143**, 106534.

13 N. C. Ou, X. Su, D. C. Bock and L. McElwee-White, *Coord. Chem. Rev.*, 2020, **421**, 213459.

14 Y. Liu, S. Cao, H. Wu, L. Zhang, B. Jia, M. Qin and X. Qu, *Ceram. Int.*, 2023, **49**, 21175.

15 (*a*) W. H. Lai, Y. H. Su, L. G. Teoh, Y. T. Tsai and M. H. Hon, *Mater. Trans.*, 2007, **48**, 1575; (*b*) M. V. Santhosh, K. S. Devaky and M. K. Jayaraj, *Mater. Today Proc.*, 2019, **25**, 183.

16 J. N. Baby, B. Akila, T. W. Chiu, S. Sakthinathan, V. Abhikha Sherlin, B. A. Zealma and M. George, *Inorg. Chem.*, 2023, **62**, 8249.

17 (*a*) N. M. Abbasi, M. Q. Farooq and J. L. Anderson, *J. Chromatogr. A*, 2021, **1643**, 462011; (*b*) T. Altamash, A. Amhamed, S. Aparicio and M. Atilhan, *Processes*, 2020, **8**, 1533; (*c*) M. Tiecco, F. Cappellini, F. Nicoletti, T. Del Giacco, R. Germani and P. Di Profio, *J. Mol. Liq.*, 2019, **281**, 423; (*d*) Y. Wang, Y. Hou, W. Wu, D. Liu, Y. Ji and S. Ren, *Green Chem.*, 2016, **18**, 3089.

18 O. Ejeromedoghene, X. Zuo, S. O. Ogungbesan, O. Oderinde, F. Yao, S. Adewuyi and G. Fu, *J. Mater. Sci.: Mater. Electron.*, 2022, **33**, 7371.

19 S. M. Park, Y. C. Nah and C. Nam, *J. Nanosci. Nanotechnol.*, 2017, **17**, 7719.

20 R. Lei, H. Zhang, H. Ni, R. Chen, H. Gu and B. Zhang, *Appl. Surf. Sci.*, 2019, **463**, 363.

21 C. Zhou, C. Sheng, L. Gao, J. Guo, P. Li and B. Liu, *Chem. Eng. J.*, 2021, **413**, 127429.

22 (*a*) P. Gupta, A. K. Sharma and I. Singh, *Ceram. Int.*, 2023, **49**, 35585; (*b*) O. Rezaee, H. Mahmoudi Chenari and F. E. Ghodsi, *J. Sol–Gel Sci. Technol.*, 2016, **80**, 109.

23 (*a*) L. Marot, J. Fleury, D. Haas, S. Iyyakkunnel, F. Sanchez, R. Steiner, D. Mathys, R. Antunes and E. Meyer, *Surf. Coat. Technol.*, 2022, **447**, 128870; (*b*) D. Nagy and S. Humphry-Baker, *Scr. Mater.*, 2022, **209**, 114373.

24 A. Shafiee, N. Rabiee, S. Ahmadi, M. Baneshi, M. Khatami, S. Iravani and R. S. Varma, *ACS Appl. Nano Mater.*, 2022, **5**, 55.

25 A. Aldrees, H. Khan, A. Alzahrani and S. Dan'azumi, *Appl. Water Sci.*, 2023, **13**, 156.

26 L. Santos, C. M. Silveira, E. Elangovan, J. P. Neto, D. Nunes, L. Pereira, R. Martins, J. Viegas, J. J. G. Moura, S. Todorovic, M. G. Almeida and E. Fortunato, *Sens. Actuators, B*, 2016, **223**, 186.

27 J. Kumari and P. Mangala, *MJChem.*, 2022, **24**, 36.

28 T. He and J. Yao, *J. Mater. Chem.*, 2007, **17**, 4547.

29 A. B. A. Kayani, S. Kuriakose, M. Monshipouri, F. A. Khalid, S. Walia, S. Sriram and M. Bhaskaran, *Small*, 2021, **17**, 2100621.

30 J. Kumari and P. Mangala, *J. Sci. Res.*, 2023, **15**, 141.

31 L. G. Carpen, M. A. Acasandrei, T. Acsente, E. Matei, I. Lungu and G. Dinescu, *Heliyon*, 2023, **9**, E13849.

32 H. H. Yu, Y. C. Chen, H. P. Su, L. Chen, H. H. Chen, K. Y. A. Lin and C. H. Lin, *Sci. Total Environ.*, 2023, **855**, 158885.

33 S. Ghazal, M. Mirzaee, M. Darroudi, Z. Sabouri and S. Khadempir, *J. Photochem. Photobiol., A*, 2024, **448**, 115323.

34 M. Selvamani, G. Krishnamoorthy, M. Ramadoss, P. K. Sivakumar, M. Settu, S. Ranganathan and N. Vengidusamy, *Mater. Sci. Eng., C*, 2016, **60**, 109.